The Astrophysical Journal, 835:182 (10pp), 2017 February 1 doi:10.3847/1538-4357/835/2/182

Multiband Observations of the Quasar PKS 2326–502 during Active and Quiescent Gamma-Ray States in 2010–2012

Michael S. Dutka[1,16], Bryce D. Carpenter[2,15], Roopesh Ojha[3,14], Justin D. Finke[4], Filippo D'Ammando[5], Matthias Kadler[6], Philip G. Edwards[7], Jamie Stevens[8], Eleonora Torresi[9], Paola Grandi[9], Roberto Nesci[10], Felicia Krauß[11], Cornelia Müller[12], Joern Wilms[13], and Neil Gehrels[2]

[1] The Catholic University of America, 620 Michigan Avenue, NE, Washington, DC 20064, USA; ditko86@gmail.com
[2] NASA Goddard Space Flight Center, Astrophysics Science Division, Code 661, Greenbelt, MD 20771, USA; carpbr01@gmail.com
[3] UMBC/NASA Goddard Space Flight Center, Astrophysics Science Division, Code 661, Greenbelt, MD 20771, USA; roopesh.ojha@gmail.com
[4] Naval Research Laboratory, Space Science Division, Code 7653, 4555 Overlook Avenue, SW, Washington, DC 20375, USA
[5] Università di Bologna Dipartimento di Fisica e Astronomia, INAF-IRA, Bologna, Italy
[6] Lehrstuhl für Astronomie, Universität Würzburg, Emil -Fischer-Straße 31, D-97074 Würzburg, Germany
[7] CSIRO Astronomy and Space Science, P.O. Box 76, Epping NSW 1710, Australia
[8] CSIRO Astronomy and Space Science, 1828 Yarrie Lake Road, Narrabri NSW 2390, Australia
[9] Istituto Nazionale di Astrofisica, (National Institute of Astrophysics) INAF-IASFBO, via Gobetti 101, I-40129 Bologna, Italia
[10] Istituto Nazionale di Astrofisica, (National Institute of Astrophysics) INAF-IAPS, via Fosso del Cavaliere 100, I-00133 Roma, Italia
[11] GRAPPA and Anton Pannekoek Institute for Astronomy, University of Amsterdam, Science Park 904, 1098 XH Amsterdam, The Netherlands
[12] Department of Astrophysics/IMAPP, Radboud University Nijmegen, P.O. Box 9010, 6500 GL, Nijmegen, The Netherlands
[13] Remeis Observatory and ECAP, Sternwartstr. 7, D-96049 Bamberg, Germany
Received 2016 January 25; revised 2016 November 9; accepted 2016 December 8; published 2017 January 30

Abstract

Quasi-simultaneous observations of the Flat Spectrum Radio Quasar PKS 2326−502 were carried out in the γ-ray, X-ray, UV, optical, near-infrared, and radio bands. Using these observations, we are able to characterize the spectral energy distribution (SED) of the source during two flaring and one quiescent γ-ray states. These data were used to constrain one-zone leptonic models of the SEDs of each flare and investigate the physical conditions giving rise to them. While modeling one flare required only changes in the electron spectrum compared to the quiescent state, modeling the other flare required changes in both the electron spectrum and the size of the emitting region. These results are consistent with an emerging pattern of two broad classes of flaring states seen in blazars. Type 1 flares are explained by changes solely in the electron distribution, whereas type 2 flares require a change in an additional parameter. This suggests that different flares, even in the same source, may result from different physical conditions or different regions in the jet.

Key words: galaxies: active – gamma rays: galaxies – quasars: individual (PKS 2326–502) – radio continuum: galaxies – ultraviolet: galaxies – X-rays: individual (PKS 2326–502)

1. Introduction

PKS 2326−502 is a Flat Spectrum Radio Quasar (FSRQ) at a tentative redshift of 0.518 (based on a single emission line, Jauncey et al. 1984). It is present in all three *Fermi* Large Area Telescope (*Fermi*-LAT) catalogs (1FGL: Abdo et al. 2010b; 2FGL: Nolan et al. 2012; 3FGL: Acero et al. 2015). In the 3FGL, it is listed as 3FGL J2329.3−4955 with a (0.1–100) GeV flux of $(25.1 \pm 0.4) \times 10^{-8}$ ph cm^{-2} s^{-1} averaged over the first four years of the *Fermi* mission. PKS 2326−502 is one of the southern hemisphere γ-ray loud active galactic nuclei (AGNs) being studied by the Tracking Active Galactic Nuclei with Austral Milliarcsecond Interferometry (TANAMI) program (Ojha et al. 2010) at radio and other wavelengths.[17]

Typically divided into BL Lacertae objects and FSRQs, blazars are the most luminous subclass of radio loud AGNs. They commonly exhibit high polarization levels and variability on a wide range of timescales and in every wavelength. Blazars often show collimated structures called jets that are thought to be powered by the accretion of material onto a spinning black hole (Blandford & McKee 1977). Jets, which can appear to be moving at superluminal speeds, are ubiquitous among radio loud AGNs and can extend for thousands of parsecs from the supermassive black hole at the center of their host galaxy. The high luminosity of blazars is a consequence of the relativistic Doppler boosting that results from the small angles between their jets and the observer's line of sight (see the review by Urry & Padovani 1995). Blazars are the largest subclass of objects detected by the LAT on the *Fermi Gamma-ray Space Telescope* (Ackermann et al. 2015).

The broadband spectral energy distribution (SED) for most blazars has a roughly "double-humped" shape, with low- and high-energy components. Blazars can be classified based on the frequency of the peak of the low-energy component in the νF_ν representation. Evidence suggests that the low-energy component is caused by synchrotron emission (Urry & Padovani 1995); therefore, we refer to this peak as the synchrotron peak. Low-synchrotron peaked (LSP) blazars have $\nu^{\rm sync}_{\rm peak}$ at $<10^{14}$ Hz; high-synchrotron peaked (HSP) blazars have $\nu^{\rm sync}_{\rm peak} > 10^{15}$ Hz; and intermediate-synchrotron peaked blazars have $\nu^{\rm sync}_{\rm peak}$ between 10^{14} and 10^{15} Hz (Abdo et al. 2010a). Almost all FSRQs, of which PKS 2326−502 is an example, are LSP blazars (Finke 2013).

The emission mechanisms responsible for the high-energy component of the blazar SED are not well established. There are

[14] Adjunct Professor, The Catholic University of America, 620 Michigan Avenue, NE, Washington, DC 20064.
[15] The Catholic University of America, 620 Michigan Avenue, NE, Washington, DC 20064.
[16] Wyle Science Technology and Engineering Group, NASA GSFC, Greenbelt, MD 20771.
[17] http://pulsar.sternwarte.uni-erlangen.de/tanami/

two broad classes of models for its origin, hadronic and leptonic (see, e.g., Böttcher 2007 for a review). Hadronic models assume that a large fraction of the jet power goes into the acceleration of protons, and then these protons and their secondaries are responsible for the high-energy emission (e.g., Mannheim & Biermann 1992). Leptonic models invoke inverse Compton scattering of seed photons by the electrons in the jet. Leptonic models can be subdivided into different types depending on the source of seed photons and the number of emitting zones (see the review by Böttcher 2007). In general, both leptonic and hadronic models can reproduce the broadband SEDs of blazars (Böttcher et al. 2013). However, hadronic models are disfavored by energetics for many FSRQs and low-peaked BL Lac objects. The jet powers required to fit the SEDs are so high that they would require an accretion rate far greater than the prevailing idea of accretion in AGNs allows (Zdziarski & Böttcher 2015; Petropoulou & Dermer 2016). Some models invoke large numbers of emitting zones (Marscher 2014) while others invoke only a single (or a few) emitting regions (Dermer et al. 2009). Leptonic models that use the synchrotron photons already present in the jet as the source of seed photons for inverse Compton scattering are referred to as synchrotron self-Compton (SSC) models (Maraschi & Tavecchio 2003). Models that use photons originating outside the jet (e.g., the accretion disk or the dust torus) are known as external Compton (EC) models (Dermer et al. 2009). Due to the variability of blazars in every observing band, modeling of these scenarios is only possible with simultaneous or close to simultaneous multiwavelength (MWL) observations in different activity states.

On 2010 August 7, the *Fermi*-LAT detected PKS 2326−502 at a daily averaged flux above 100 MeV of $(1.1 \pm 0.3) \times 10^{-6}$ ph cm^{-2} s^{-1}, a factor of 15 brighter than the average over the first 11 months of *Fermi*-LAT operations (D'Ammando 2010) and a factor of 4.4 brighter than the 3FGL average flux. Follow-up X-ray, UV and optical observations were made by the *Swift* XRT and UVOT on 2010 August 18. Two years later, on 2012 June 27, PKS 2326−502 was detected with a daily averaged flux of $(1.4 \pm 0.3) \times 10^{-6}$ ph cm^{-2} s^{-1} by the *Fermi*-LAT. This was a factor of 11 greater than the average flux over the first two years of the mission (D'Ammando & Torresi 2012) and a factor of 5.6 greater than the 3FGL flux. Again *Swift* made follow-up observations on 2012 June 29 (MJD 56107) providing X-ray, UV, and optical measurements. Additional observations were made in the optical band by the ANDICAM at Cerro Tololo on 2012 June 30 (MJD 56108) and the Rapid Eye Mount 0.6 m telescope in La Silla, Chile on 2012 July 01 (MJD 56109) and 02 (MJD 56110). Radio measurements were made by the Australia Telescope Compact Array on 2012 June 29 (MJD 56107) as part of the TANAMI monitoring program. In order to investigate the high-energy emission from PKS 2326−502, we have defined two flaring and one quiescent γ-ray states based on the *Fermi*-LAT light curve (Figure 1).

This paper is organized as follows. In Section 2, we discuss the LAT analysis, followed by Sections 3–5 describing observations at X-ray, ultraviolet, optical, and radio wavelengths respectively. In Section 6, we describe our modeling and discuss what our observations and modeling suggest. The conclusions can be found in Section 7. We assume $H_0 = 70$ km s^{-1} Mpc^{-1}, $\Omega_m = 0.3$, and $\Omega_\lambda = 0.7$.

2. LAT Observations

The *Fermi*-LAT (Atwood et al. 2009) is one of the two instruments on board the *Fermi Gamma-ray Space Telescope*. It is a γ-ray pair production detector providing unprecedented all-sky spatial and energy resolution in the 100 MeV–300 GeV band. It typically operates in an all-sky survey mode and its 2.5 steradian field of view allows it to monitor the entire sky once every 3 hr, enabling rapid response to extraordinary γ-ray flaring activity. Thus *Fermi*-LAT is an ideal instrument to trigger near simultaneous broadband coverage.

An LAT γ-ray light curve of PKS 2326-502 has been created from 2009 February 21 (MJD 54883) to 2012 December 5 (MJD 56266) in order to determine the duration of the flaring periods and select a quiescent state. For each of these states spectral fitting was used to determine the flux in multiple energy bands. The first flare lasted from 2010 July 31 (MJD 55408) to 2010 September 29 (MJD 55468; hereafter Flare "A") and the second from 2012 June 25 (MJD 56103) to 2012 July 05 (MJD 56113) (hereafter Flare "B"). In order to provide a baseline to compare the flaring states, observations that were performed during a γ-ray quiescent state from 2011 December 18 (MJD 55913) to 2012 January 29 (MJD 55955; hereafter period "Q") are also considered.

The light curve, shown in Figure 1, was created with data in the 100 MeV to 300 GeV energy range using the adaptive binning approach described in Lott et al. (2012). A caveat with this method is that fluxes for nearby point sources are not accounted for. However, PKS 2326−502 is well outside the Galactic plane and has no bright nearby sources (nearest source is 1°.2, the next closest is more than 2° away) which makes it an excellent source for the adaptive binning method. The adaptive binning method varies the time bin size so that each bin has a fixed flux error of 15%. The variability timescales (the time for the flux to rise or fall by a factor of two) found from the light curve are 1.4×10^5 s during flare A and 1.8×10^5 s during flare B. These timescales were calculated by the time difference between points that had a factor of two difference in flux within the flaring period. Because this technique uses the actual data points and does not extrapolate between them, it produces only estimated upper limits. Any shorter timescale variability than the time bin size is lost. The parameters in Table 3 were selected to fit the SED data, but are consistent with these timescales because the measured timescales are only upper limits. We have estimated the variability timescales with a uniform binned light curve, but the results were less constraining.

For both the light curve and spectral fitting, events above a zenith angle of 100° were cut and a rocking angle cut of 52° was applied to avoid contamination from the Earth limb. The Galactic diffuse emission and the isotropic background were accounted for using the models gal_2yearp7v6_v0.fits and iso_p7v6source.txt[18] with fixed normalizations. The analysis was done using Fermi science tools version 09-27-00 with instrument response function P7SOURCE_V6.

LAT spectral analysis was conducted separately on two flaring states (flare A and flare B), and for the quiescent period Q. The "source" event class was selected and data extracted from a circular region of interest (ROI) of 10° centered on PKS 2326−502. The starting spectral model of the source used a power law with a spectral index of 2.24 and a flux of 1.2×10^{-7} ph cm^{-2} s^{-1}. These starting parameters are the averages from the Fermi 2FGL catalog. These parameters were refitted for each period based on the data. The model of the ROI contains the 2FGL information on all sources within 20° of the source. Sources within 10° had the normalization parameter free and the index fixed to values determined by a

[18] http://fermi.gsfc.nasa.gov/ssc/data/access/lat/BackgroundModels.html

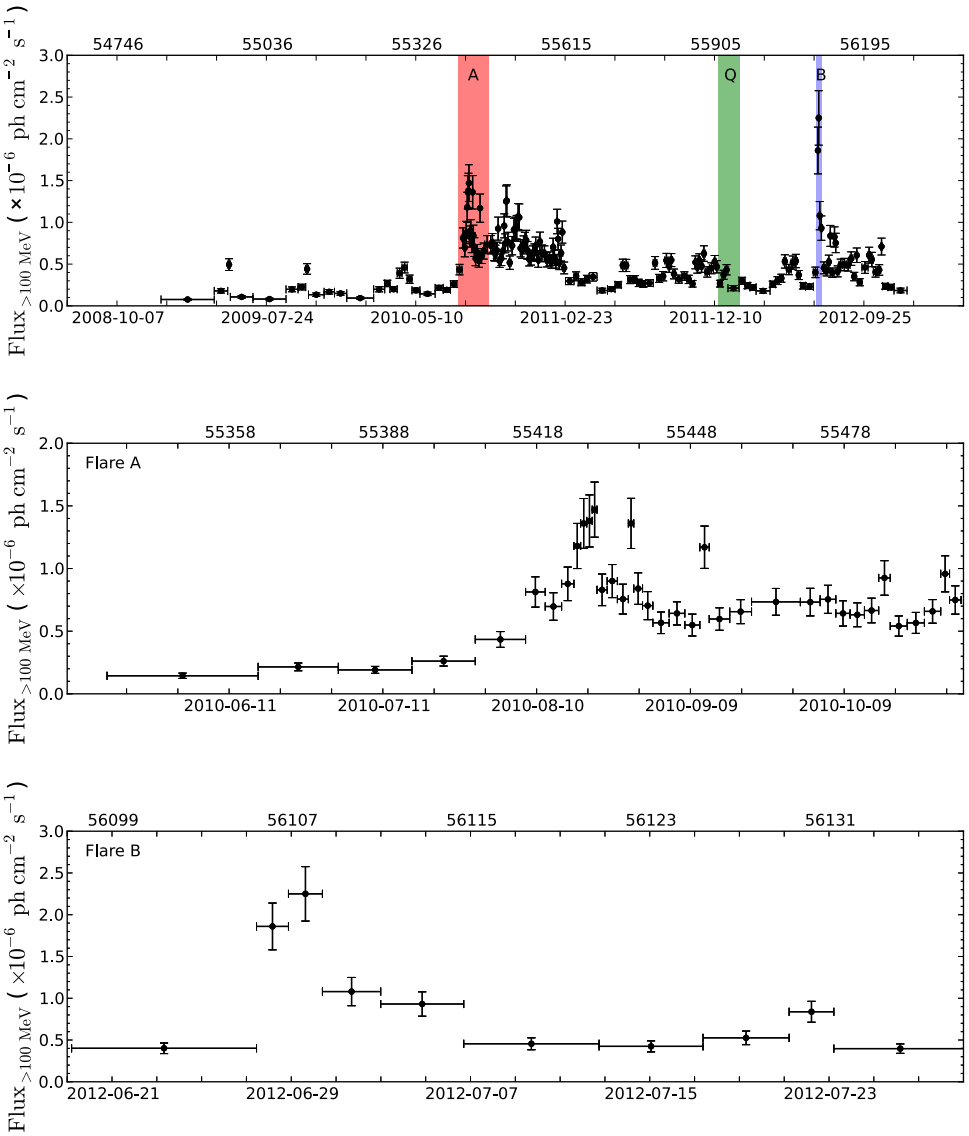

Figure 1. Top panel is the *Fermi*-LAT adaptively binned γ-ray light curve in the 100 MeV to 300 GeV energy range for PKS 2326−502. It covers the period from 2009 February 21 (MJD 54883) to 2012 December 05 (MJD 56266). The bin sizes are set such that a constant flux uncertainty of 15% is maintained. Three different states of the source are selected and their MWL SEDs are modeled. The long active state is from 2010 July 31 (MJD 55408) to 2010 September 29 (MJD 55468; flare A, in red), the quiescent state from 2011 December 18 (MJD 55913) to 2012 January 29 (MJD 55955; period Q, in green), and a short, high peaked, flaring state from 2012 June 25 (MJD 56103) to 2012 July 05 (MJD 56113; flare B, in purple). The middle panel shows a zoomed view of Flare A from 2010 May 10 (MJD 55326) to 2010 November 1 (MJD 55501). The bottom panel shows Flare B from 2012 June 19 (MJD 56097) to 2012 July 29 (MJD 56137). Note that the three plots all have different time axes.

likelihood analysis across the entire energy range during each period. For those sources outside 10°, both parameters were fixed to the 2FGL values. The spectral indices for other sources were held fixed for the determination of the spectral points and the light curve. The fluxes were determined by likelihood analyses using the `gtlike` tool of the Fermi Science Tools.

Analysis was conducted using several different spectral shapes for the γ-ray data (power law, broken power law, and log parabola).[19] Flare A was best fit by the power-law model, showing no significant curvature. In flare B, the power-law fit was slightly worse than the other models, with a preference of 3σ significance for the log parabola over the power law. The quiescent state showed no significant preference, with differences of 1 and 2σ between the models' significance.

[19] http://fermi.gsfc.nasa.gov/ssc/data/analysis/scitools/xml:model_defs.html

The two flaring states differ in length: flare A showed increased emission for an extended period of time (approximately 200 days) as can be seen in Figure 1, whereas flare B showed a sharp peak after which the flux very quickly returned to its previous state (within 60 days). Flare A had an average spectral index of 2.23 ± 0.03, a peak flux of $(1.47 \pm 0.22) \times 10^{-6}$ ph cm^{-2} s^{-1} and average flux of $(8.82 \pm 1.32) \times 10^{-7}$ ph cm^{-2} s^{-1}. During flare B, the average spectral index was 1.99 ± 0.05 with peak flux $(2.25 \pm 0.33) \times 10^{-6}$ ph cm^{-2} s^{-1} and average flux $(1.53 \pm 0.23) \times 10^{-6}$ ph cm^{-2} s^{-1}. Period Q had a spectral index of 2.25 ± 0.06 and average flux $(3.2 \pm 0.5) \times 10^{-7}$ ph cm^{-2} s^{-1}. To determine individual spectral points, an analysis was run on energy bins using the spectral index found by analysis over the entire LAT energy spectrum. These spectra can be seen in Figure 2. The size of the bins varies due to the photon statistics available for each period.

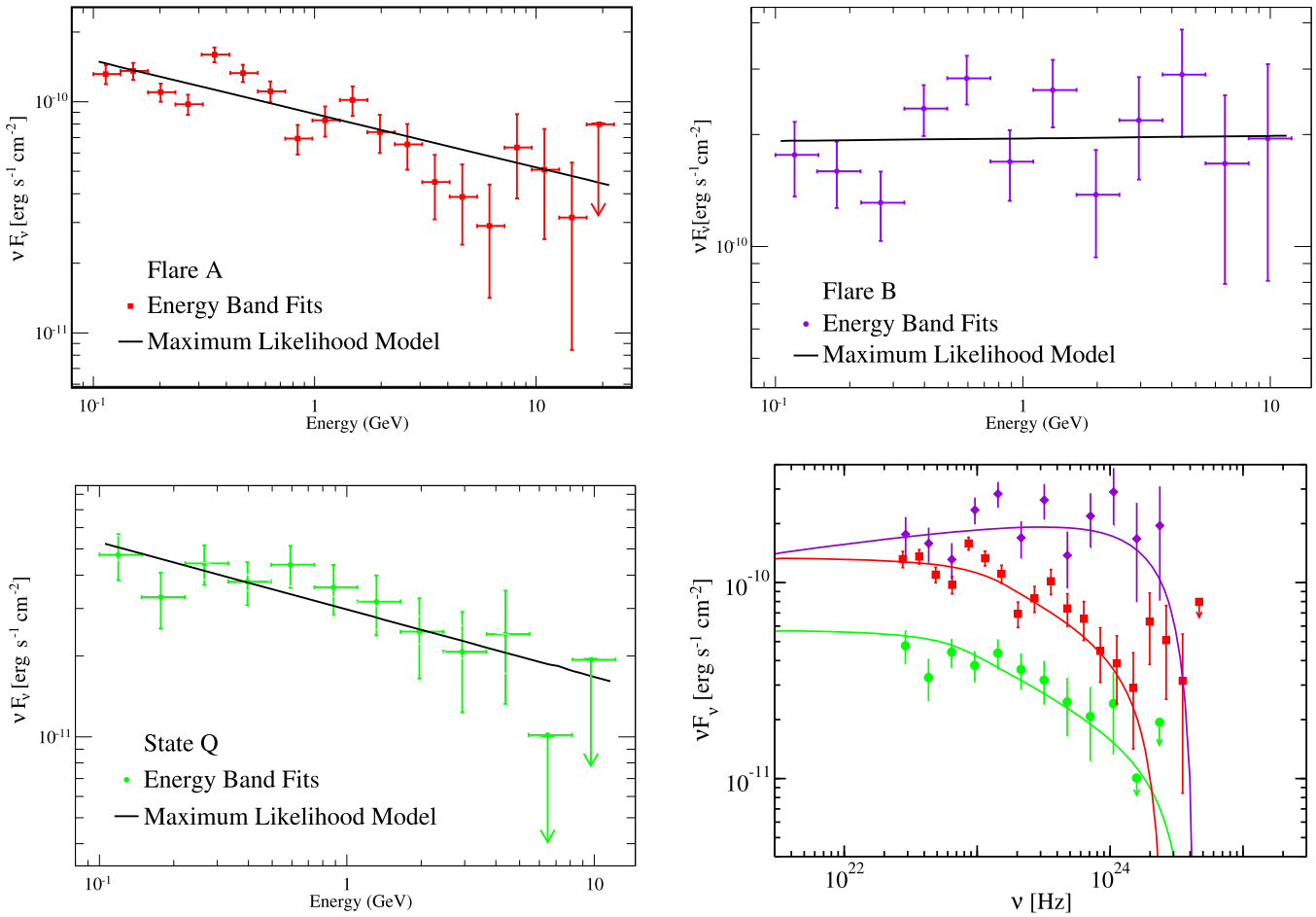

Figure 2. γ-ray SEDs of PKS 2326−502. The top left, top right, and bottom left plots show the SED during flare A, flare B, and period Q, respectively. The black line on each plot shows the power-law fit. The bottom right plot shows the data points for all three states, along with the overall multiwavelength SED models described in Section 6.

3. *Swift* Observations

The *Swift* observatory (Gehrels et al. 2004) was designed as a rapid response mission for expeditious follow-up of γ-ray bursts. Its quick slew rate and the availability of Target of Opportunity observations make *Swift* a powerful tool for the study of AGN flares detected by the *Fermi*-LAT. During this observing campaign, we used the data from two of the instruments on board *Swift*, the UltraViolet and Optical Telescope (UVOT), and the X-Ray Telescope (XRT).

Observations of PKS 2326−502 were made during flare A, the quiescent state, and flare B, on 2010 August 18 (MJD 55426), 2011 December 30 (MJD 55925) and 31 (MJD 55926), and 2012 June 29 (MJD 56107), respectively. During flare A, the XRT observed for 4.7 ks and UVOT observations were made with the V, B, U, W1, M2, and W2 filters. For the period Q, the XRT took 2.7 ks of data and the UVOT observed with the W1, M2, and W2 filters. During flare B the XRT observed for 2.0 ks and UVOT observed with the U and W2 filters.

The XRT spectrum was fit in the 0.3–10 keV range and the fit used an absorbed power law with an $N_{\rm H}$ column density of $1.18 \times 10^{20}\,{\rm cm}^{-2}$ (Kalberla et al. 2005). The XRT data were processed by using the `xrtpipeline` of the `HEASoft`[20] package (v6.14) with standard procedures, filtering, and screening criteria. Considering the low number of photons collected (<200 counts), the spectra were rebinned with a minimum of 1 count per bin and we performed the fit with the Cash statistic (Cash 1979). Source events were extracted from a circular region with a radius of 20 pixels (1 pixel $\sim$ 2.36 arcsec), while background events were extracted from a circular region with a radius of 50 pixels, far away from bright sources. Ancillary response files were generated with `xrtmkarf` and account for different extraction regions, vignetting, and point-spread function corrections. We used the spectral redistribution matrices in the calibration database maintained by HEASARC.[21]

UVOT data were analyzed with the `uvotsource` task included in the `HEASoft` package (v6.14). Source counts were extracted from a circular region of 5 arcsec radius centered on the source, while background counts were derived from a circular region with 10 arcsec radius in a nearby source-free region. The central wavelengths of the filters are V: 5468 Å, B: 4392 Å, U: 3465 Å, UVW1: 2600 Å, UVM2: 2246 Å, and UVW2: 1928 Å. Galactic extinction was corrected for using the method from Fitzpatrick (1999) and the method described in Predehl & Schmitt (1995) was used to calculate the extinction parameter $E(B-V)$ from the $N_{\rm H}$ column density. The $N_{\rm H}$ Column density is 1.18×10^{20} cm^{-2}. The relation from Predehl & Schmitt (1995) is $E(B-V) = 5.3 \times 10^{21}\,N_{\rm H}$ giving an $E(B-V)$ value of 0.022.

[20] http://heasarc.nasa.gov/lheasoft/

[21] http://heasarc.nasa.gov/

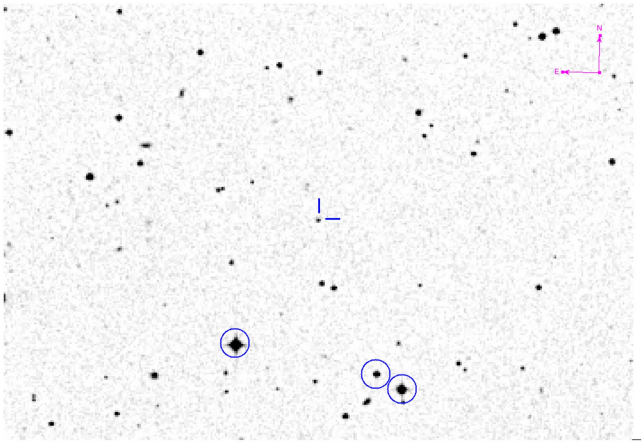

Figure 3. Optical image from DSS showing the finder and comparison stars, which are circled.

4. Optical/NIR Observations

Regular observations of many *Fermi*-LAT and TANAMI blazars are made by the Small and Moderate Aperture Research Telescope System (SMARTS; Bonning et al. 2012). Providing optical and IR photometric data, SMARTS uses the ANDICAM mounted on the 1.3 m telescope located at the Cerro Tololo Inter-American Observatory. The ANDICAM uses a dichroic to take simultaneous optical and infrared data with a CCD and an HgCdTe array. The IR exposures can be dithered during the optical exposure through the use of a moveable mirror. SMARTS observed PKS 2326−502 on 2012 June 30 (MJD 56108) in the R band contemporaneously to flare B. The other two periods were not observed by SMARTS.

The 0.6 m Rapid Eye Mount (REM; Chincarini et al. 2003) telescope is primarily designed to provide rapid response to γ-ray bursts detected by *Swift* and other satellites. It is located on the La Silla premises of the ESO Chilean Observatory. REM observed PKS 2326−502 in the J and K bands on 2012 July 01 (MJD 56109) and the H band on 2012 July 02 (MJD 56110) contemporaneously to flare B. Photometric data from REM were analyzed using the IRAF/Apphot package.[22] Photometric measurements were made on the source as well as several nearby stars (within 3 arcmin) surrounding the source in the sky (Table 2 and Figure 3). A linear fit between the instrumental magnitudes of these stars and their catalog magnitudes was used to find the magnitude of PKS 2326 −502. Error estimates were obtained from the root-mean-square deviation of the reference stars from the best-fit line.

These observations were all corrected for Galactic extinction with the values from Schlafly & Finkbeiner (2011), as found on the NASA Extragalactic Database.[23] The values were 0.028, 0.009, 0.006, and 0.004 for the R, J, H, and K bands, respectively. The magnitudes were converted to fluxes using photometric zero points from Frogel et al. (1978), Bessell et al. (1998), and Elias et al. (1982). A description of the SMARTS data reduction can be found in Bonning et al. (2012).

The *Wide-field Infrared Survey Explorer* (*WISE*; Wright et al. 2010) is an all-sky survey mission in the mid-infrared that operated between 2009 January (MJD 54840) and 2010 October (MJD 55470). It took images that were 47 arcminutes in width, every 11 s. It was capable of imaging near-infrared (3.4 and 4.6 μm) and mid-infrared (12 and 22 μm) bands. *WISE* made an observation of PKS 2326−502 on 2010 July 25 (MJD 55402) that was not simultaneous with flare A, flare B, or period Q. However, since the source seemed to be in a low γ-ray state at that time, five days before the start of flare A, we tentatively include the data as part of period Q. This observation was made at all four wavebands. The data are drawn from the *WISE* Preliminary Data Release.[24] The fluxes and the corresponding magnitudes can be found in Table 1.

Table 1
WISE Results

WISE Bandpass Wavelength (μm)	Magnitude	Flux (mJy)
3.4	13.42 ± 0.03	1.36 ± 0.03
4.6	12.19 ± 0.03	2.26 ± 0.05
12	9.00 ± 0.02	7.88 ± 0.17
22	6.45 ± 0.05	21.67 ± 0.98

Table 2
Coordinates (J2000) of the Comparison Stars Used in the REM Photometry

R.A.	Decl.
23:29:29.01	−49:57:40.1
23:29:14.91	−49:58:08.0
23:29:12.38	−49:58:20.2

5. Radio Observations

PKS 2326−502 is observed by the Australia Telescope Compact Array (ATCA) at several radio frequencies as part of the TANAMI blazar monitoring program (Stevens et al. 2012). Data from this monitoring were available during the quiescent state (2012 January 15, MJD 55941) and flare B (2012 June 29, MJD 56107). No ATCA data were available during flare A. The ATCA is an array consisting of 6 × 22 m radio antennas with adjustable baselines and a longest baseline of 6 km. The array configuration is changed every few weeks. However, as PKS 2326−502 is a point source even for ATCA's longest baseline, ATCA's configuration does not affect our observations. The receivers at ATCA can be quickly changed allowing observations to be made over a large range of frequencies in a short period of time. The array is located in northern New South Wales, at a latitude of −30° and altitude 237 m above sea level. During the quiescent state ATCA observed at 5, 9, 17, 19, 38, and 40 GHz. The 2012 flare has observations at 9, 17, 19, 38, and 40 GHz. Snapshot observations of PKS 2326−502 of several minutes duration were made at each frequency, and calibrated against the ATCA primary flux calibrator PKS 1934−638. Observations at 38/40 GHz are preceded by a scan on a bright nearby AGNs to apply corrections to the global pointing model. Data reduction was carried out in the standard manner with the miriad software package.[25]

6. Results

Using the data described above, MWL SEDs were constructed for both flaring states and the quiescent state. Then we modeled the three states with a one-zone leptonic model (Finke et al. 2008; Dermer et al. 2009). These models assume most

[22] ftp://iraf.noao.edu/ftp/docs/apuser.ps.Z
[23] https://ned.ipac.caltech.edu/
[24] http://wise2.ipac.caltech.edu/docs/release/prelim/
[25] http://www.atnf.csiro.au/computing/software/miriad/

Table 3
Model Parameters for the SED Shown in Figure 4

Parameter	Symbol	Quiescent	Flare A	Flare B
Redshift	z	0.518	0.518	0.518
Bulk Lorentz Factor	Γ	30	30	30
Doppler factor	δ_D	30	30	30
Magnetic Field [G]	B	0.50	0.50	0.50
Variability Timescale [s]	t_v	4.6×10^4	4.6×10^4	1.3×10^5
Comoving radius of blob [cm]	R'_b	2.7×10^{16}	2.7×10^{16}	7.7×10^{16}
Electron Spectral Index 1	p_1	2.0	2.0	2.0
Electron Spectral Index 2	p_2	3.0	3.0	2.8
Electron Spectral Index 3	p_3	3.6	3.6	n/a
Minimum Electron Lorentz Factor	$\gamma'_{\rm min}$	2.0	4.0	4.0
Break Electron Lorentz Factor 1	$\gamma'_{\rm brk1}$	1.0×10^2	1.0×10^2	1.0×10^2
Break Electron Lorentz Factor 2	$\gamma'_{\rm brk2}$	5.1×10^2	6.7×10^3	n/a
Maximum Electron Lorentz Factor	$\gamma'_{\rm max}$	4.0×10^3	3.0×10^3	4.0×10^3
black hole Mass [$M_\odot$]	$M_{\rm BH}$	1.0×10^9	1.0×10^9	1.0×10^9
Accretion disk luminosity [erg s^{-1}]	$L_{\rm disk}$	3.0×10^{44}	3.0×10^{44}	3.0×10^{44}
Inner accretion disk radius [R_g]	$R_{\rm in}$	6.0	6.0	6.0
Accretion Efficiency	η	1/12	1/12	1/12
Seed photon source energy density [erg cm^{-3}]	$u_{\rm seed}$	1.8×10^{-4}	1.8×10^{-4}	1.8×10^{-4}
Seed photon source photon energy	$\epsilon_{\rm seed}$	9.0×10^{-7}	9.0×10^{-7}	9.0×10^{-7}
Dust Torus luminosity [erg s^{-1}]	$L_{\rm dust}$	1.1×10^{43}	1.1×10^{43}	1.1×10^{43}
Dust Torus radius [cm]	$R_{\rm dust}$	5.6×10^{17}	5.6×10^{17}	5.6×10^{17}
Jet Power in Magnetic Field [erg s^{-1}]	$P_{j,B}$	1.3×10^{45}	1.3×10^{45}	1.0×10^{46}
Jet Power in Electrons [erg s^{-1}]	$P_{j,e}$	2.1×10^{45}	4.1×10^{45}	1.6×10^{45}

of the radiation comes from a small spherical, isotropic emission component of radius R'_b moving at relativistic speed βc giving it a Lorentz factor $\Gamma = [1 - \beta^2]^{-1/2}$ moving at an angle θ to the line of sight, so that its Doppler factor $\delta_D = [1 - \beta \cos(\theta)]^{-1}$. The emitting region has a non-thermal electron population that creates synchrotron emission through interactions with a magnetic field of strength B and Compton scatters these synchrotron photons (synchrotron self-Compton or SSC), and a radiation field external to the jet (external Compton or EC). The external isotropic radiation field was assumed to be monochromatic and isotropic in the frame of the host galaxy and black hole, though we chose its parameters consistent with a dust torus. An isotropic, monochoromatic radiation field is a good representation for a more complicated dust torus geometry as long as the emitting region is closer to the black hole than the dust torus radius (e.g., Finke 2016). PKS 2326−502 has an uncertain redshift of $z = 0.518$ based on a weak detection of a single emission line identified with Mg II λ2798 (Jauncey et al. 1984). We use this redshift for our modeling, but one should keep its uncertainty in mind. The size of the emitting region was constrained by the time it takes for the flux to change by a factor of 2, found to be about a day from the γ-ray light curve (Figure 1). The fastest variability observed was about 1.6 days, making the 1 day estimate for the SED model compatible with the observations. Estimates from the light curve data can be found in Section 2 and model parameters from the SED data can be found in Table 3.

The modeling results are presented in Figure 4 and Table 3 and the data are contained in Table 4 in the appendix. A detailed explanation of the model parameters can be found in Dermer et al. (2009); there is a short description of them given in Table 3. We chose a relatively weak multi-color accretion disk (Shakura & Sunyaev 1973) to model the optical portion of the SED in the quiescent state, which is consistent with the lack of features in the source's optical spectrum (Jauncey et al. 1984). The black hole's mass is not known, but we chose a standard value of 10^9 $M_\odot$, so that the optical SED data points in the quiescent state are consistent with the Shakura-Sunyaev disk emission (Figure 4).

We found that all three states could be modeled with a broken power-law electron distribution. However, with this model, the SED in the 10^{19}–10^{21} Hz (40 keV−4 MeV) range does not very closely resemble the SED of other FSRQs, producing a flat spectrum in νF_ν (i.e., $\nu F_\nu \propto \nu^0$). It is particularly apparent in blazars that have been detected by *Swift*-BAT (e.g., Ackermann et al. 2014) and *NuSTAR* (e.g., Ajello et al. 2016; Paliya et al. 2016; Sbarrato et al. 2016) that this type of SED shape is not observed here. Consequently, we chose to model the quiescent and the flare A SED with a double broken power law. In this case, its electron distribution is

$$N_e(\gamma) \propto \begin{cases} \gamma'^{-p_1} & \gamma'_1 < \gamma' < \gamma'_{\rm brk1} \\ \gamma'^{-p_2} & \gamma'_{\rm brk1} < \gamma' < \gamma'_{\rm brk2} \\ \gamma'^{-p_3} & \gamma'_{\rm brk2} < \gamma' < \gamma'_2 \end{cases} \quad (1)$$

where γ' is the electron Lorentz factor in the frame comoving with the blob. This type of electron distribution is not without precedence, e.g., a double broken power-law electron distribution was used by D'Ammando et al. (2013) to model the SED of PKS 0537−441. Here, it also allowed us to obtain models closer to equipartition. This electron distribution could be tested by observations by *NuSTAR*, which would constrain the energy range that necessitates the double broken power law. Flare B required only a broken power-law electron distribution

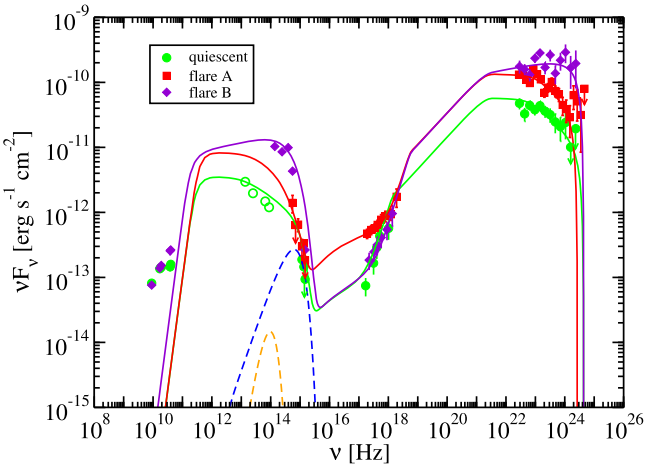

Figure 4. Broadband SED model for PKS 2326−502. The data are modeled with a one-zone leptonic model of blazar emission (Finke et al. 2008). The low-energy component is modeled as a combination of synchrotron emission from the jet and thermal emission from the accretion disk. A double broken power law is used to model the electron distribution during the quiescent state flare A. A change in the size of the emitting region is used to model flare B. The smaller dashed yellow-orange curve represents emission from the dust torus (1.8×10^3 K) and the larger dashed blue curve is accretion disk emission. The high-energy component is explained by inverse Compton scattering of dust torus photons by electrons within the jet. Hollow circles represent non-simultaneous data.

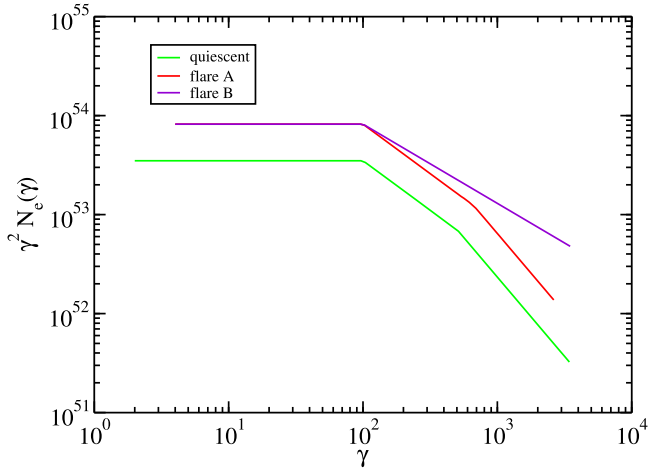

Figure 5. Electron distributions used in our modeling of the quiescent state, flare A, and flare B.

to explain the X-ray to γ-ray portion of the SED. The electron distributions used in our modeling can be found in Figure 5.

We found that the quiescent state and flare A could be modeled by varying only the electron distribution between states. This is similar to the flaring states found in PKS 0537−441 (D'Ammando et al. 2013), "flare B" from PKS 2142−75 (Dutka et al. 2013), and the flaring states of 4C+21.35 (Ackermann et al. 2014). Modeling flare B by varying only the electron distribution would result in the SSC emission over-producing X-rays. Therefore, the variation in another parameter is necessary. We chose to change the variability timescale t_v, which has the effect of expanding the size of the emitting region in the model (R_b'). The larger variability timescale is still consistent with the light curve presented in Figure 1.

According to the relation from Ghisellini & Tavecchio (2008), the broad-line region (BLR) radius, $R_{\rm BLR}$ is given by,

$$R_{\rm BLR,17} = L_{\rm disk,45}^{1/2}. \quad (2)$$

so that in our case, $R_{\rm BLR} = 5.5 \times 10^{16}$ cm. Here we use the notation $A = 10^x A_x$ and cgs units. This value would not be consistent with the size of the emitting region inferred from the variability timescale, though we note that size is only a soft upper limit based on the most rapid changes seen in the light curve, not the most rapid possible changes. Also, the disk luminosity is not well-constrained from the SED. We still chose to model the source with the dust torus as the source of seed photons, though one should keep the caveats in mind. The energy density from the dust torus with temperature T, which reprocesses a fraction ξ of the disk luminosity, assuming the radiation is dominated by the inner dust radius, is

$$u_{\rm dust} = 2.4 \times 10^{-5} \xi_{\rm dust,-1} T_3^{5.2} \text{ erg cm}^{-3} \quad (3)$$

(Nenkova et al. 2008; Sikora et al. 2009). The model has dimensionless seed photon energy and energy density $\epsilon_{\rm seed} = 9.0 \times 10^{-7}$ and $u_{\rm seed} = 1.8 \times 10^{-4}$ erg cm^{-3}, respectively. This implies $T_3 = 1.8$, $\xi_{-1} = 0.35$ giving dust torus luminosity and radius $L_{\rm dust} = 1.1 \times 10^{43}$ erg s^{-1} and $R_{\rm dust} = 5.6 \times 10^{17}$ cm, respectively. Assuming a conical jet, the jet half-opening angle must be greater than $\alpha = R_b'/R_{\rm dust} = 2.^\circ 8$, which is consistent with measurements of jet opening angles in other FSRQs inferred from VLBI observations (Jorstad et al. 2005).

The accretion power in this model is $P_{\rm acc} = L_{\rm disk}/\eta = 3.6 \times 10^{45}$ erg s^{-1}. The models for the three states give results that imply the electron energy density is almost in equipartition with the magnetic energy density. The total jet powers, $P_j = P_{j,e} + P_{j,B}$ make up a large fraction of the accretion powers, ranging from $P_j/P_{\rm acc} = 0.95$ for the quiescent state to $P_j/P_{\rm acc} = 3.2$ for flare B. The jet seems to be highly efficient for this source, with the jet power even exceeding the power from accretion only during the flares. This may be possible in magnetically arrested accretion onto a black hole with nearly maximal spin (Tchekhovskoy et al. 2011). However, there are large uncertainties in the jet power from the modeling, and the disk luminosity is not well-constrained. Better data in the optical band, especially a better optical spectrum, could tighten the constraints on the disk luminosity.

7. Discussions and Conclusions

In order to study the origins of the high-energy emission, observations and archival data from *Fermi*, *Swift*, SMARTS, REM, *WISE*, and ATCA were used to construct the MWL SEDs of PKS 2326−502 during quiescent and two flaring γ-ray states. Period Q was a period of "average" γ-ray activity for PKS 2326−502 and was used to provide a baseline with which to compare flare A and flare B. A one-zone leptonic model can appropriately describe the SEDs constrained by these data.

Modeling flare A and flare B required different changes to the parameters of the SED model that describes the state Q. Flare A required changing only the electron distribution. However, the increased emission during flare B could not be explained by changes in the electron distribution alone and required a change in the size of the emitting region as well. This fits with a previous classification scheme for blazar flares (Dutka et al. 2013). Within this scheme AGNs exhibit flares of

two types. Type 1 flares (like flare A) are those that show changes in the SED from a quiescent state, which can be explained entirely by modifying the electron distribution. Flare B is a type 2 flare. These require a change in the electron distribution but that is not sufficient; a change to either the magnetic field, Doppler factor, or the size of the emitting region must be made to match the emission across the SED. If the magnetic field or Doppler factor only were varied, another parameter would need to be varied also; therefore, we chose the simplest route, only varying one parameter.

As is seen here with PKS 2326−502 that both types of flares can occur from the same source. These classes can each be divided into subclasses. Type 1a shows increased emission at both the optical and γ-ray wavelengths, type 1b only shows an increase in the γ-ray band. X-ray emission can see either an increase or not for type 1 flares. Type 2a features flaring in the optical and γ-ray but not in the X-ray, type 2b displays flaring in optical, X-ray and γ-ray. Here we would classify flare A as a type 1a and flare B as a type 2b flare.

We expect to improve on this classification scheme and to gain new insights into the high-energy emission processes in PKS 2326−502 through observations of additional active states. VLBI observations of PKS 2326−502 are being made by the TANAMI program using the Long Baseline Array based in Australia. These will allow us to determine the jet kinematics, including a more direct measure of the Doppler factor. VLBI monitoring can show us the emergence of new jet components. The emergence of jet components has been found to be associated with γ-ray flares (Wehrle & Zook 1994; Jorstad et al. 2001); and in fact a recent analysis indicates that two-thirds of gamma-ray flares are associated with the ejection of jet components (Marscher et al. 2012). Broadband observations of flares combined with VLBI monitoring could determine if new components emerge with specific types of flares. ALMA observations will constrain the sub-millimeter region of future SEDs leading to a much better determination of the synchrotron peak. Observations with *NuSTAR* in the hard X-ray regime (3–79 keV) would help constrain the SED in the region where the power-law breaks occur. More broadband, quasi-simultaneous observations of other AGNs are essential to improving and verifying the tentative classification scheme outlined above, thus helping solve the puzzle of high-energy emission in blazars.

8. Summary

We studied two major flares from PKS 2326−502 in 2010 and 2012 as shown in Figure 1. We constructed SEDs using broadband data from the two flares and a single selected γ-ray quiescent state. The quiescent state was used as a baseline for investigating the two flares.

The flares showed distinct behavior in time and the shape of their γ-ray and broadband SEDs. Within the scope of a tentative classification scheme being developed, we classify flare A as a type 1a and flare B as a type 2b flare. Flare A was also different from flare B in that it was the beginning of a long, sustained period of high flux, whereas flare B showed a very sharp peak and a faster return to average fluxes.

This emerging classification scheme may allow us to gain additional physical insight into the processes that cause blazar flares. Our models suggest that these processes are not uniform, and that they can arise from different physical conditions. This sort of behavior could be expected from a turbulent, outflowing plasma. Type 1 flares, where changes to the electron distribution are sufficient to cause the flare, may result from electrons moving into or out of the emitting region. Alternatively, the electrons within the emitting region could experience a bulk acceleration. The γ-ray emitting region moving outward along the jet might change the electron distribution as well. Type 2 flares could be explained by shocks changing the shape of the emitting region. A compression, or expansion, of the emitting region could have an effect on the magnetic energy density. The diversity in the behavior of simultaneous SEDs may allow us to probe the behavior of jets at scales that are too small to resolve with current observational techniques.

This research was funded in part by NASA through *Fermi* Guest Investigator grants NNH09ZDA001N, NNH10ZDA001N, and NNH12ZDA001N. This research was supported by an appointment to the NASA Postdoctoral Program at the Goddard Space Flight Center, administered by Oak Ridge Associated Universities through a contract with NASA. This publication makes use of data products from the Wide-field Infrared Survey Explorer, which is a joint project of the University of California, Los Angeles, and the Jet Propulsion Laboratory/California Institute of Technology, funded by the National Aeronautics and Space Administration. The Australia Telescope Compact Array is part of the Australia Telescope National Facility, which is funded by the Commonwealth of Australia for operation as a National Facility managed by CSIRO. This research has made use of data from the NASA/IPAC Extragalactic Database (NED), operated by the Jet Propulsion Laboratory, California Institute of Technology, under contract with the National Aeronautics and Space Administration; and the SIMBAD database (operated at CDS, Strasbourg, France). This research has made use of NASA's Astrophysics Data System. This research has made use of the United States Naval Observatory (USNO) Radio Reference Frame Image Database (RRFID). This paper has made use of up-to-date SMARTS optical/near-infrared light curves that are available at http://www.astro.yale.edu/smarts/glast/home.php. F.K. acknowledges funding from the European Unions Horizon 2020 research and innovation programme under grant agreement No 653477.

The *Fermi*-LAT Collaboration acknowledges generous ongoing support from a number of agencies and institutes that have supported both the development and the operation of the LAT as well as scientific data analysis. These include the National Aeronautics and Space Administration and the Department of Energy in the United States, the Commissariat à l'Energie Atomique and the Centre National de la Recherche Scientifique/Institut National de Physique Nucléaire et de Physique des Particules in France, the Agenzia Spaziale Italiana and the Istituto Nazionale di Fisica Nucleare in Italy, the Ministry of Education, Culture, Sports, Science and Technology (MEXT), High Energy Accelerator Research Organization (KEK) and Japan Aerospace Exploration Agency (JAXA) in Japan, and the KA Wallenberg Foundation, the Swedish Research Council and the Swedish National Space Board in Sweden. Additional support for science analysis during the operations phase is gratefully acknowledged from the Istituto Nazionale di Astrofisica in Italy and the Centre National d'Études Spatiales in France.

Facilities: ATCA, *Fermi*, *Swift*, SMARTS, *WISE*.

Appendix

Table 4
Broadband SEDs Data Points as shown in Figure 4

Flare A		
Frequency (Hz)	Flux (erg cm^{-2} s^{-1})	Error (erg cm^{-2} s^{-1})
5.550E+14	1.40E–12	4.22E–13
6.925E+14	6.38E–13	Upper Limit
8.563E+14	6.50E–13	1.46E–13
1.157E+15	2.99E–13	8.52E–14
1.345E+15	3.34E–13	Upper Limit
1.475E+15	1.82E–13	Upper Limit
1.898E+17	4.73E–13	7.66E–14
2.611E+17	5.37E–13	8.24E–14
3.421E+17	5.72E–13	8.89E–14
4.316E+17	6.44E–13	1.11E–13
5.694E+17	7.73E–13	1.51E–13
7.955E+17	8.78E–13	1.62E–13
1.219E+18	9.35E–13	1.83E–13
1.905E+18	1.74E–12	5.48E–13
2.756E+22	1.32E–10	1.25E–11
3.665E+22	1.36E–10	1.13E–11
4.875E+22	1.10E–10	9.95E–12
6.484E+22	9.74E–11	9.66E–12
8.624E+22	1.58E–10	1.17E–11
1.147E+23	1.33E–10	1.14E–11
1.525E+23	1.11E–10	1.16E–11
2.029E+23	6.92E–11	1.02E–11
2.699E+23	8.30E–11	1.25E–11
3.589E+23	1.02E–10	1.49E–11
4.773E+23	7.38E–11	1.39E–11
6.349E+23	6.54E–11	1.46E–11
8.444E+23	4.49E–11	1.39E–11
1.123E+24	3.88E–11	1.47E–11
1.494E+24	2.90E–11	1.48E–11
1.987E+24	6.33E–11	2.51E–11
2.642E+24	5.08E–11	2.54E–11
3.514E+24	3.15E–11	2.30E–11
4.674E+24	7.98E–11	Upper Limit
Flare B		
Frequency (Hz)	Flux (erg cm^{-2} s^{-1})	Error (erg cm^{-2} s^{-1})
9.000E+09	7.61E–14	3.80E–15

Table 4
(Continued)

Flare A		
1.700E+10	1.39E–13	1.39E–14
1.900E+10	1.53E–13	1.53E–14
3.800E+10	2.56E–13	3.84E–14
4.000E+10	2.64E–13	3.96E–14
1.380E+14	1.03E–11	4.86E–13
2.438E+14	8.54E–12	4.03E–13
3.928E+14	9.91E–12	4.96E–13
5.550E+14	4.31E–12	1.53E–13
1.475E+15	2.65E–13	2.05E–14
2.225E+17	1.85E–13	5.50E–14
3.228E+17	2.47E–13	7.34E–14
4.195E+17	3.17E–13	9.98E–14
5.731E+17	4.09E–13	1.29E–13
9.019E+17	5.44E–13	1.71E–13
1.365E+18	9.57E–13	3.45E–13
2.896E+22	1.76E–10	4.00E–11
4.321E+22	1.59E–10	3.23E–11
6.448E+22	1.31E–10	2.78E–11
9.623E+22	2.35E–10	3.68E–11
1.436E+23	2.84E–10	4.25E–11
2.143E+23	1.69E–10	3.65E–11
3.198E+23	2.64E–10	5.44E–11
4.772E+23	1.38E–10	4.43E–11
7.122E+23	2.19E–10	6.72E–11
1.063E+24	2.90E–10	9.33E–11
1.586E+24	1.67E–10	8.80E–11
2.367E+24	1.95E–10	1.14E–10
Period Q		
Frequency (Hz)	Flux (erg cm^{-2} s^{-1})	Error (erg cm^{-2} s^{-1})
5.500E+09	4.92E–14	2.46E–15
9.000E+09	8.14E–14	4.07E–15
1.700E+10	1.36E–13	1.36E–14
1.900E+10	1.43E–13	1.43E–14
3.800E+10	1.45E–13	2.18E–14
4.000E+10	1.58E–13	2.38E–14
1.157E+15	1.88E–13	3.16E–14
1.345E+15	1.45E–13	3.45E–14
1.475E+15	9.37E–14	Upper Limit
1.692E+17	7.44E–14	2.34E–14

Table 4
(Continued)

Flare A		
3.155E+17	1.66E–13	5.56E–14
4.063E+17	2.89E–13	9.67E–14
5.102E+17	4.33E–13	1.45E–13
1.017E+18	5.69E–13	1.90E–13
2.886E+22	4.76E–11	9.28E–12
4.307E+22	3.28E–11	7.77E–12
6.427E+22	4.42E–11	7.49E–12
9.591E+22	3.78E–11	6.90E–12
1.431E+23	4.37E–11	7.73E–12
2.136E+23	3.60E–11	7.61E–12
3.187E+23	3.18E–11	8.01E–12
4.756E+23	2.46E–11	8.15E–12
7.098E+23	2.08E–11	8.40E–12
1.059E+24	2.41E–11	1.09E–11
1.581E+24	1.01E–11	Upper Limit
2.359E+24	1.94E–11	Upper Limit

References

Abdo, A. A., Ackermann, M., Agudo, I., et al. 2010a, ApJ, 716, 30
Abdo, A. A., Ackermann, M., Ajello, M., et al. 2010b, ApJS, 188, 405
Acero, F., Ackermann, M., Ajello, M., et al. 2015, ApJS, 218, 23
Ackermann, M., Ajello, M., Allafort, A., et al. 2014, ApJ, 786, 157
Ackermann, M., Ajello, M., Atwood, W. B., et al. 2015, ApJ, 810, 14
Ajello, M., Ghisellini, G., Paliya, V. S., et al. 2016, ApJ, 826, 76
Atwood, W. B., Abdo, A. A., Ackermann, M., et al. 2009, ApJ, 697, 1071
Bessell, M. S., Castelli, F., & Plez, B. 1998, A&A, 333, 231
Blandford, R. D., & McKee, C. F. 1977, MNRAS, 180, 343
Bonning, E., Urry, C. M., Bailyn, C., et al. 2012, ApJ, 756, 13
Böttcher, M. 2007, Ap&SS, 309, 95
Böttcher, M., Reimer, A., Sweeney, K., & Prakash, A. 2013, ApJ, 768, 54
Cash, W. 1979, ApJ, 228, 939
Chincarini, G., Zerbi, F., Antonelli, A., et al. 2003, Msngr, 113, 40
D'Ammando, F. 2010, ATel, 2783, 1
D'Ammando, F., Antolini, E., Tosti, G., et al. 2013, MNRAS, 431, 2481
D'Ammando, F., & Torresi, E. 2012, ATel, 4225, 1
Dermer, C. D., Finke, J. D., Krug, H., & Böttcher, M. 2009, ApJ, 692, 32
Dutka, M. S., Ojha, R., Pottschmidt, K., et al. 2013, ApJ, 779, 174
Elias, J. H., Frogel, J. A., Matthews, K., & Neugebauer, G. 1982, AJ, 87, 1029
Finke, J. D. 2013, ApJ, 763, 134
Finke, J. D. 2016, ApJ, 830, 94
Finke, J. D., Dermer, C. D., & Böttcher, M. 2008, ApJ, 686, 181
Fitzpatrick, E. L. 1999, PASP, 111, 63
Frogel, J. A., Persson, S. E., Matthews, K., & Aaronson, M. 1978, ApJ, 220, 75
Gehrels, N., Chincarini, G., Giommi, P., et al. 2004, ApJ, 611, 1005
Ghisellini, G., & Tavecchio, F. 2008, MNRAS, 387, 1669
Jauncey, D. L., Batty, M. J., Wright, A. E., Peterson, B. A., & Savage, A. 1984, ApJ, 286, 498
Jorstad, S. G., Marscher, A. P., Lister, M. L., et al. 2005, AJ, 130, 1418
Jorstad, S. G., Marscher, A. P., Mattox, J. R., et al. 2001, ApJ, 556, 738
Kalberla, P. M. W., Burton, W. B., Hartmann, D., et al. 2005, A&A, 440, 775
Lott, B., Escande, L., Larsson, S., & Ballet, J. 2012, A&A, 544, A6
Mannheim, K., & Biermann, P. 1992, A&A, 253, L21
Maraschi, L., & Tavecchio, F. 2003, ApJ, 593, 667
Marscher, A. P. 2014, ApJ, 780, 87
Marscher, A. P., Jorstad, S. G., Agudo, I., MacDonald, N. R., & Scott, T. L. 2012, Fermi & Jansky Proc.—eConf C1111101, arXiv:1204.6707
Nenkova, M., Sirocky, M. M., Ivezić, Ž., & Elitzur, M. 2008, ApJ, 685, 147
Nolan, P. L., Abdo, A. A., Ackermann, M., et al. 2012, ApJS, 199, 31
Ojha, R., Kadler, M., Böck, M., et al. 2010, A&A, 519, A45
Paliya, V. S., Parker, M. L., Fabian, A. C., & Stalin, C. S. 2016, ApJ, 825, 74
Petropoulou, M., & Dermer, C. D. 2016, ApJL, 825, L11
Predehl, P., & Schmitt, J. H. M. M. 1995, A&A, 293, 889
Sbarrato, T., Ghisellini, G., Tagliaferri, G., et al. 2016, MNRAS, 462, 1542
Schlafly, E. F., & Finkbeiner, D. P. 2011, ApJ, 737, 103
Shakura, N. I., & Sunyaev, R. A. 1973, A&A, 24, 337
Sikora, M., Stawarz, Ł., Moderski, R., Nalewajko, K., & Madejski, G. M. 2009, ApJ, 704, 38
Stevens, J., Edwards, P. G., Ojha, R., et al. 2012, Fermi & Jansky Proc.—eConf C1111101, arXiv:1205.2403
Tchekhovskoy, A., Narayan, R., & McKinney, J. C. 2011, MNRAS, 418, L79
Urry, C. M., & Padovani, P. 1995, PASP, 107, 803
Wehrle, A. E., Zook, A. C., Unwin, S. C., Urry, C. M., & Madejski, G. 1994, in High Energy Astrophysics Division Meeting of the American Astronomical Society, The Multimission Perspective (Washington, DC: AAS), 27
Wright, E. L., Eisenhardt, P. R. M., Mainzer, A. K., et al. 2010, AJ, 140, 1868
Zdziarski, A. A., & Böttcher, M. 2015, MNRAS, 450, L21